Doppler wind measurements in Neptune's stratosphere with ALMA

Óscar Carrión-González, Raphael Moreno, Emmanuel Lellouch, Thibault Cavalié, Sandrine Guerlet, Gwenaël Milcareck, Aymeric Spiga, Noé Clément, Jérémy Leconte

Astronomy & Astrophysics

LETTER TO THE EDITOR

Doppler wind measurements in Neptune's stratosphere with ALMA

Óscar Carrión-González[1], Raphael Moreno[1], Emmanuel Lellouch[1], Thibault Cavalié[2,1], Sandrine Guerlet[3,1], Gwenaël Milcareck[3], Aymeric Spiga[3], Noé Clément[2], and Jérémy Leconte[2]

[1] LESIA, Observatoire de Paris, Université PSL, CNRS, Sorbonne Université, Université Paris Cité, 5 place Jules Janssen, 92195 Meudon, France
e-mail: oscar.carrion.gonzalez@gmail.com, oscar.carrion@obspm.fr

[2] Laboratoire d'Astrophysique de Bordeaux, Univ. Bordeaux, CNRS, B18N, Allée Geoffroy Saint-Hilaire, 33615 Pessac, France

[3] Laboratoire de Météorologie Dynamique/Institut Pierre-Simon Laplace (LMD/IPSL), Sorbonne Université, CNRS, École Polytechnique, Institut Polytechnique de Paris, École Normale Supérieure (ENS), PSL Research University, Paris, France

Received 7 April 2023 / Accepted 10 May 2023

ABSTRACT

Context. Neptune's tropospheric winds are among the most intense in the Solar System, but the dynamical mechanisms that produce them are still unclear. Measuring wind speeds at different pressure levels may help shed light on the atmospheric dynamics of the planet.

Aims. The goal of this work is to directly measure winds in Neptune's stratosphere with ALMA Doppler spectroscopy.

Methods. We derived the Doppler lineshift maps of Neptune at the CO(3-2) and HCN(4-3) lines at 345.8 GHz ($\lambda \sim 0.87$ mm) and 354.5 GHz (0.85 mm), respectively. For that purpose, we used spectra obtained with ALMA in 2016 and recorded with a spatial resolution of $\sim 0.37''$ on Neptune's $2.24''$ disk. After subtracting the planet's solid rotation, we inferred the contribution of zonal winds to the measured Doppler lineshifts at the CO and HCN lines. We developed an MCMC-based retrieval methodology to constrain the latitudinal distribution of wind speeds.

Results. We find that CO(3-2) and HCN(4-3) lines probe the stratosphere of Neptune at pressures of $2^{+12}_{-1.8}$ mbar and $0.4^{+0.5}_{-0.3}$ mbar, respectively. The zonal winds at these altitudes are less intense than the tropospheric winds based on cloud tracking from Voyager observations. We find equatorial retrograde (westward) winds of -180^{+70}_{-60} m s^{-1} for CO, and -190^{+90}_{-70} m s^{-1} for HCN. Wind intensity decreases towards mid-latitudes and wind speeds at 40°S are -90^{+50}_{-60} m s^{-1} for CO and -40^{+60}_{-80} m s^{-1} for HCN. Wind speeds become 0 m s^{-1} at about 50°S. We find that the circulation reverses to a prograde jet southwards of 60°S. Overall, our direct stratospheric wind measurements match previous estimates from stellar occultation profiles and expectations based on thermal wind equilibrium.

Conclusions. These are the first direct Doppler wind measurements performed on the Icy Giants, opening up a new method for the study and monitoring of their stratospheric dynamics.

Key words. planets and satellites: atmospheres – planets and satellites: gaseous planets – radiative transfer

1. Introduction

Voyager 2 measurements of Neptune's atmosphere have revealed some of the most intense zonal winds ever measured in the Solar-System planets (Hammel et al. 1989; Smith et al. 1989). This was done by tracking cloud motions in images of Voyager's ISS instrument, thereby constraining Neptune's winds to be -400 m s^{-1} (retrograde) at the equator, with a prograde jet of about $+250$ m s^{-1} at latitude 70°S (Limaye & Sromovsky 1991; Sromovsky et al. 1993). Subsequent cloud-tracking measurements with the *Hubble* Space Telescope (Sromovsky et al. 2001a,b) and ground-based observatories with adaptive optics (Fitzpatrick et al. 2014; Tollefson & Pater 2018) have confirmed this general wind pattern (Fletcher et al. 2020).

However, cloud-tracking methods generally lack an accurate constraint of the atmospheric altitudes probed by the observations. Although clouds are mostly expected to be located in the upper troposphere ($\sim$100 mbar–1 bar), determining the exact cloud-top pressure levels requires multiple-scattering radiative-transfer computations. These are highly dependent on the assumed optical properties of the atmospheric aerosols and on the assumed vertical distribution of gaseous species and aerosols

(e.g. Luszcz-Cook et al. 2016). Furthermore, cloud pressure levels have been found to vary with latitude by about an order of magnitude (Irwin et al. 2011, 2016; Hueso et al. 2017). Even clouds at similar latitudes have been found to be located at pressure levels across such a varied range of pressure levels as 30–300 mbar (de Pater et al. 2014).

Above the cloud level, wind information has been derived primarily from the thermal wind equation that relates the latitudinal temperature gradient to the vertical wind shear. Initially, temperature fields from Voyager/IRIS spectra were used for this (Conrath et al. 1989). Later, additional ground-based thermal observations became available (Fletcher et al. 2014). At tropospheric levels, these data consistently indicate a warm equator, cool mid-latitudes, and a warmer south pole. The thermal wind equation (which cannot be applied at the equator) implies decaying winds with altitude at low latitudes ($-30°$ to $30°$) and essentially altitude-independent winds at mid-to-high southern latitudes. Relatively small changes were found in the predicted circulation pattern from 1989 to 2003 (southern summer solstice), except near the south pole, which was found to be anomalously warm (by $\sim$5 K) in 2003 (Orton et al. 2007).
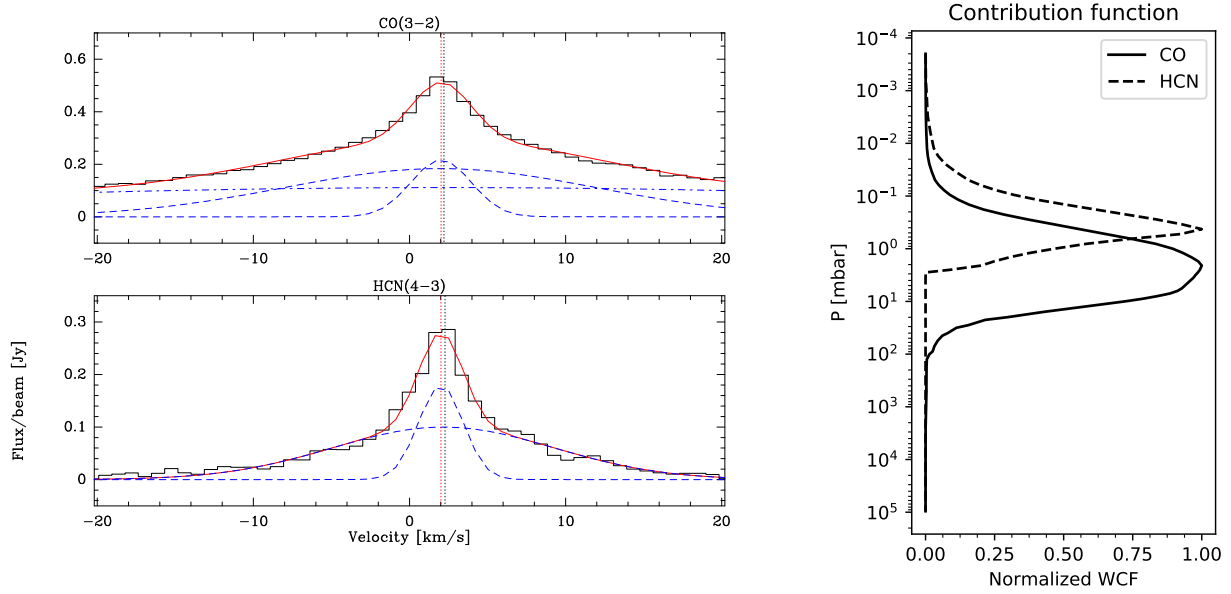
Fig. 1. Example of measured spectra (left column) of CO(3-2) and HCN(4-3) lines (black) at the position of the sky western equatorial limb, at an offset from Neptune centre (−1.1″, 0.0″). Individual Gaussian fit components with FWHMs of about 4, 20, 80 km s^{-1} are shown in dashed blue and their sum in red. Also shown: the beam-convolved solid body velocity (black dotted line) and the fit velocity (red dotted line). The difference of these two velocities allows us to derive the Doppler winds. Right: normalized wind contribution functions (WCF) at the limb for each molecule.

Additional wind measurements with other techniques were performed for a reduced number of latitudes. French et al. (1998) measured stratospheric winds from three stellar occultations over 1985–1989, constraining the wind-distorted shape of the planet. They inferred that wind speeds at the 0.38 mbar level are 0.6±0.2 times those of Voyager cloud-tracking from Sromovsky et al. (1993). Also, they found tentative evidence of winds at 0.7 μbar further decaying to ∼0.17 times the tropospheric values. This was the first direct evidence for the decay of winds above the tropopause, with an estimated wind shear in agreement with that inferred from Voyager temperature fields at deeper levels.

In this work, we aim to directly measure Neptune's stratospheric winds based on Doppler lineshift measurements of CO and HCN lines with the Atacama Large Millimeter/submillimeter Array (ALMA). Millimetric and submillimetric measurements have already been used to directly measure the winds in the atmospheres of Venus (e.g., Lellouch et al. 2008, and references therein), Mars (Lellouch et al. 1991; Cavalié et al. 2008; Moreno et al. 2009), Jupiter (Cavalié et al. 2021), Saturn (Benmahi et al. 2022), and Titan (Moreno et al. 2005; Lellouch et al. 2019; Cordiner et al. 2020). No such analysis has been available for the Icy Giants to date. Besides probing the stratospheres of these planets, which is otherwise challenging, an advantage of the technique is that it is insensitive to aerosols, reducing considerably the uncertainties on the probed levels.

2. Observations

We observed Neptune on April 30, 2016, over 20 min on-source, with 41 antennas of the ALMA interferometer in the C36-2/3 hybrid configuration, yielding an angular resolution of about 0.37″. The spectral setup included the CO(3-2) line at 345.7959899 GHz and the HCN(4-3) line at 354.5054773 GHz, as well as the CS(7-6) line at 342.883 GHz (whose detection was reported in Moreno et al. 2017), with a spectral resolution of 1 MHz. The bandpass, amplitude, and phase calibration procedure of the CS visibilities was described in Moreno et al. (2017), and we applied the same calibration procedure to the CO and HCN data using the ALMA/CASA data reduction software.

The resulting calibrated visibilities were then exported into the GILDAS package with the following aims: (i) to apply a self-calibration technique using Neptune's continuum to improve the image quality (ii) to perform the imaging and deconvolution using the Högbom algorithm (Högbom 1974). We obtained a synthetic elliptical beam (robust weighting 0.5) of 0.39″×0.34″ (polar angle (PA) of −47°) for CO and 0.37″×0.35″ (PA = −82°) for HCN. The planet's angular diameter was 2.24″. This yields a spatial resolution of about 20° at the equator. The resulting spectral maps are shown Fig. A.1 with signal-to-noise ratio (S/N) at line peak at the limbs of about 150 and 50, respectively, for CO and HCN. The final clean images were built with a sampling of 0.05″ over −1.4″ and +1.4″ (3136 points).

An example of the observed lines is shown in Fig. 1. The detailed analysis of the lineshapes in terms of spatial and vertical distribution of temperature, as well as CO and HCN, is left for future work. For the purpose of measuring winds from line central positions, we performed Gaussian fits: we used three-Gaussian fits for CO (with initial FWHM of 4, 20, and 80 km s^{-1}) and two-Gaussian fits for HCN (with initial FWHM of 3 and 16 km s^{-1}) as shown in Fig. 1. We retained the narrowest component to measure the Doppler lineshift. The high S/N in our maps allowed us to derive the Doppler lineshifts with an averaged velocity accuracy of 25 and 37 m s^{-1}, respectively, for CO and HCN (Fig. 2, right column).

3. Model

3.1. Radiative transfer

We used the same Neptune radiative transfer model described in Moreno et al. (2017), along with their thermal profile and their
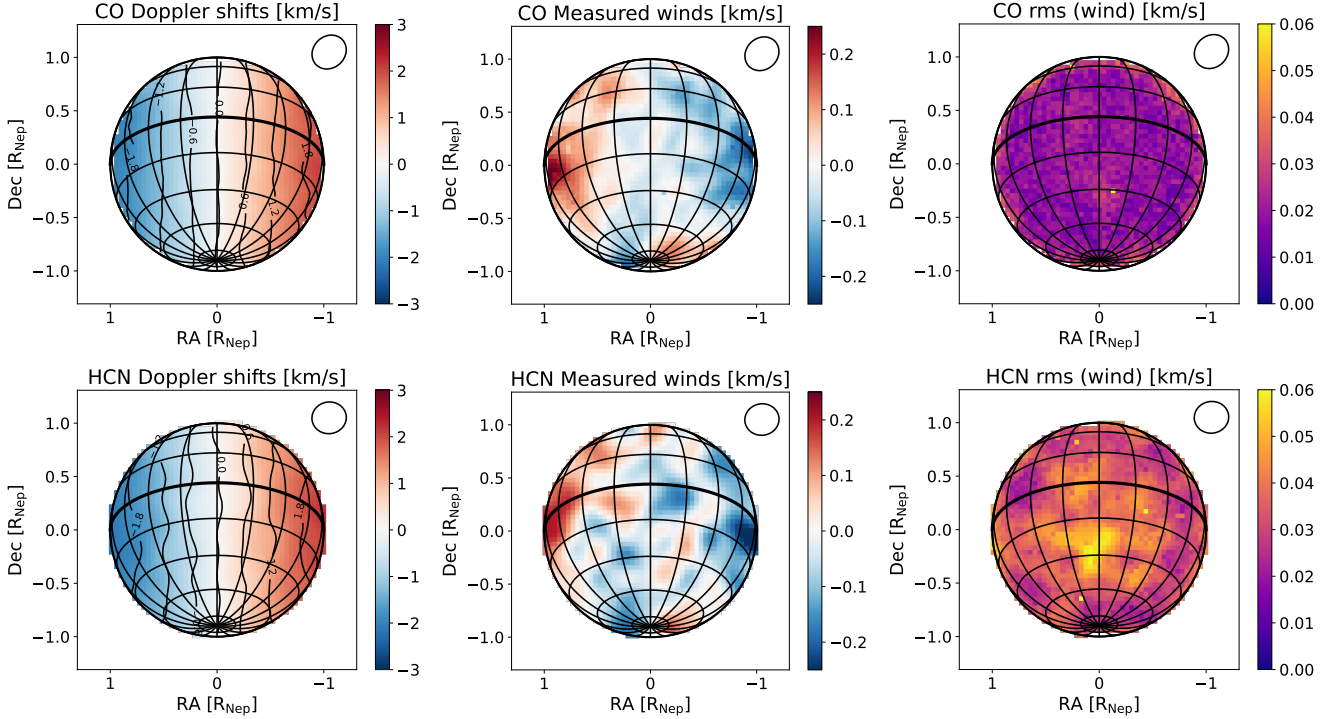
Fig. 2. ALMA Doppler measurements for the CO(3-2) line (top row) and the HCN(4-3) line (bottom row). Left: measured Doppler lineshift. Middle: line-of-sight winds, after subtracting the solid-body rotation. Right: root mean square (rms) of the measured winds. Top-right ellipse in each subplot shows the synthetic beam. Latitudes are shown in 20° steps, with the equator displayed as the thicker line.

CO and HCN vertical distributions, to model the spectral lines of CO and HCN, as well as to compute the wind weighting function shown in Fig. 1. Wind weighting functions account for the spectrally-dependent wind information content of each channel within lines (see e.g., Lellouch et al. 2019), and were convolved by the beam. At the limb (where most of the wind information comes from) CO lines probe the $2^{+12}_{-1.8}$ mbar level and HCN lines probe the $0.4^{+0.5}_{-0.3}$ mbar level.

3.2. Wind retrieval methodology

In order to interpret the measured Doppler lineshifts, we developed a retrieval framework for the wind profiles based on the Markov chain Monte Carlo (MCMC) emcee sampler (Foreman-Mackey et al. 2013). The observed lineshifts correspond to the sum of the line-of-sight Doppler displacement due to the planetary rotation and the winds. The planet rotation was modelled as solid-body rotation at the altitude of the 1 mbar level above the local planet radius. Although somewhat different rotation periods have been proposed (Helled et al. 2010; Karkoschka 2011), a period of 16.11 h (Warwick et al. 1989; Lecacheux et al. 1993) is adopted here to enable comparisons with the Voyager winds.

We parameterized the wind profiles (W), assumed to be purely zonal, as a polynomial function depending on the latitude (ϕ, given in degrees) that takes the form:

$$W = \sum_n (a_n \times \phi^n),\qquad(1)$$

and we used emcee to explore the parameter space described by the coefficients a_n, given in m s^{-1}. The box priors which set the limits of the parameter space were $[-500, 500]$ for a_0 and $[-1, 1]$ for the other coefficients. We tested polynomial orders from 0 to 5 for the wind parameterization, as discussed in Sect. 4.

The MCMC sampler tests points of the n-dimensional parameter space of a_n coefficients. For each test point, we computed the wind profile at latitudes $\phi \in [-90°, 90°]$ and the resulting wind map, with a pixel stepsize of 0.05″. To simulate the line-of-sight Doppler lineshifts at each point of the map, we projected the zonal winds onto the planet geometry, accounting for the sub-observer latitude of 26.2°S. We then weighted the modelled lineshifts by the local intensity of the CO (resp. HCN) line and convolved by the ALMA beam, following a similar procedure to Lellouch et al. (2019). After adding the contribution of the solid body rotation, the test wind map (W_{test}) was compared with the one measured by ALMA (W_{ALMA}) for the molecule under study (Fig. 2, middle) by means of the χ^2 figure of merit:

$$\chi^2 = \sum_{i=1}^{N_{\text{p}}} \left(\frac{W_{\text{test}} - W_{\text{ALMA}}}{\text{rms}_{\text{ALMA}}} \right)^2,\qquad(2)$$

where rms_{ALMA} is the 1-σ error of the ALMA measurement for the molecule under study (Fig. 2, rightmost column) and N_{p} is the number of pixels in the wind map.

We used 50 chains (or "walkers") to simultaneously explore the parameter space independently in order to avoid possible χ^2 local minima. The 50 walkers ran for up to 5×10^4 steps, with a convergence criterion to stop the run at a number of steps larger than 50 times the autocorrelation time (τ, see Foreman-Mackey et al. 2013, for details). This convergence criterion ensures that the sampling of the parameter space has been completed and the sampled test points are effectively independent (Goodman & Weare 2010). For the analysis of each retrieval run, we discarded the samples of the first τ steps ("burn-in phase").

For each retrieval run, we defined the ensemble of good fits as those sampled wind profiles with a χ^2 value in the 68.3% (i.e.,

Table 1. Polynomial coefficients of the best fits to the CO and HCN zonal wind measurements.

	a_0	a_1	a_2	a_3	a_4
CO best fit	$-1.81 \times 10^{+2}$	8.76×10^{-1}	6.04×10^{-2}	-7.44×10^{-4}	-5.50×10^{-6}
CO upper error	$-1.29 \times 10^{+2}$	-3.25×10^{-1}	5.42×10^{-2}	1.41×10^{-3}	2.72×10^{-5}
CO lower error	$-2.28 \times 10^{+2}$	8.53×10^{-1}	1.42×10^{-2}	-2.89×10^{-3}	-3.06×10^{-5}
HCN best fit	$-1.87 \times 10^{+2}$	-8.11×10^{-1}	8.39×10^{-2}	4.53×10^{-4}	2.14×10^{-6}
HCN upper error	$-1.07 \times 10^{+2}$	-7.46×10^{-1}	6.61×10^{-2}	1.29×10^{-3}	2.11×10^{-5}
HCN lower error	$-2.40 \times 10^{+2}$	4.92×10^{-1}	7.47×10^{-2}	-1.79×10^{-3}	-2.92×10^{-5}

Notes. Also given: the coefficients that approximate the envelope of good fits to a fourth-order polynomial.

1-σ) confidence level. That is as follows, with χ^2 verifying:

$$\chi^2 - \chi^2_{\min} \leq C \times \frac{\chi^2_{\min}}{N} \times f_{\text{oversampling}}. \quad (3)$$

Here, $\chi^2_{\min}$ is the minimum χ^2 value among all the samples in the run, and $\chi^2_{\min}/N$ is the reduced value of $\chi^2_{\min}$, with N equal to the degrees of freedom of the retrieval ($N = N_p - n$). The factor $f_{\text{oversampling}} = \text{Area}_{\text{beam}}/\text{Area}_{\text{pixel}}$ accounts for the fact that with a spatial sampling step of 0.05″ and a beam of 0.37″, the measurements are considerably oversampled, and the number of independent measurements is $N_p/f_{\text{oversampling}}$. The coefficient C denotes the 1-σ confidence region in the n-dimensional parameter space, where n is the number of a_n coefficients in the polynomial fit. For polynomial orders 0–5, C is 1.0, 2.3, 3.53, 4.72, 5.89, and 7.04, respectively (see Ch. 15.6 in Press et al. 2007).

4. Results

With the method above, we carried out wind retrievals for the CO and HCN measurements. We ran retrievals for wind parameterizations with polynomials of orders between 0 and 5. Previous cloud-tracking studies had generally assumed latitudinally symmetric wind profiles and thereby omitted odd polynomial orders (Sromovsky et al. 1993; Fitzpatrick et al. 2014; Tollefson & Pater 2018). However, the spatial resolution achieved in our data is potentially sensitive to latitudinal wind asymmetries. Therefore, we kept odd polynomial orders in our retrievals.

The retrieval results for CO and HCN with polynomial fits of orders 0–5 are shown in Fig. B.1. The sixth-order polynomial fit to Voyager's cloud-tracking measurements (Sromovsky et al. 1993) is shown for comparison. For each tested polynomial order, we include in Fig. B.1 the map of residuals between the observed Doppler lineshifts and the best-fitting model (solid rotation plus wind) to assess the variation of fit quality as a function of polynomial degree. For both CO and HCN, we find that the value of χ^2/N is practically the same for retrievals of orders 3, 4, and 5. This implies that these polynomials are similarly able to fit the measurements at the latitudes we are sensitive to. Indeed, the three parameterizations retrieve similar values of the zonal winds at latitudes over 20°N to 70°S.

Given Neptune's sub-observer latitude of 26.2°S and projection effects, the wind information is restricted to latitudes southward of 40°N. In addition, the beam size of 0.37″ prevents the retrieval of detailed information at southern polar latitudes. Angular speed considerations indicate that the wind speed should theoretically be zero at the pole. We find that this constraint is met within the error bars for the fourth- and fifth-order polynomial fits. Therefore, the order $n = 4$ represents a good

compromise between the model's mathematical complexity and physical realism, and we adopted it as the reference wind parameterization.

Figure 3 shows the retrieved wind profiles for the reference $n = 4$ parameterization. Table 1 shows the polynomial coefficients for CO and HCN best-fit wind profile, as well as the coefficients that parameterize the envelope of good solutions – namely, those verifying Eq. (3) – using a fourth-order polynomial fit. Figure 3 also shows our retrieved wind measurements at 0°, 20°, and 70°S as a function of pressure. For reference, the plot includes previously reported zonal winds (see discussion in Sect. 5).

At the equator, we retrieved retrograde (westward) zonal winds of -180^{+70}_{-60} m s^{-1} from CO measurements and -190^{+90}_{-70} m s^{-1} from HCN. We find a decrease in the wind intensity towards mid-latitudes. At 20°S, wind speeds are -170^{+50}_{-40} m s^{-1} for CO (-140^{+60}_{-60} m s^{-1} for HCN) and at 40°S, they are -90^{+50}_{-60} m s^{-1} for CO (-40^{+60}_{-80} m s^{-1} for HCN). Winds continue along this trend towards southern latitudes, becoming 0 m s^{-1} at about 50°S. At 70°S, winds are prograde (eastward) although uncertainties are larger (180^{+130}_{-110} m s^{-1} for CO, and 180^{+110}_{-140} m s^{-1} for HCN). Further south than 70°S, the winds remain unconstrained due to the limited spatial resolution. Wind speeds in the observable northern-hemisphere latitudes are compatible, within errors, with a symmetric wind profile. At 20°N, zonal winds are -150^{+30}_{-80} m s^{-1} for CO and -170^{+80}_{-50} m s^{-1} for HCN. Additional measurements will be needed to confirm this behaviour, eventually when regions further north become observable.

5. Discussion

Our results offer a new method for probing Neptune's stratospheric winds and wind shear, while also yielding latitudinal information. In Fig. 3, we plot the representative values of wind speeds at 0°, 20°, and 70°S from CO and HCN in the context of previous measurements. Within the errors, our values agree with the thermal wind values calculated by Fletcher et al. (2014), both with respect to their reanalysis of the Voyager/IRIS data and for their 2003 Keck data. Our retrieved winds also agree with the wind speed at 0.38 mbar derived by French et al. (1998) from stellar occultations. A comparison with the Voyager 2 cloud-tracking winds (Sromovsky et al. 1993) also confirms a decay of the wind intensity with latitude, as well as a lower value of the wind shear at high latitudes. Although the various observations pertain to different epochs, our results validate predictions of the thermal wind equation and argue for a preservation of the general circulation pattern over the 28 year interval (~60 deg in heliocentric longitude) spanned by the data around the 2005 southern summer solstice.
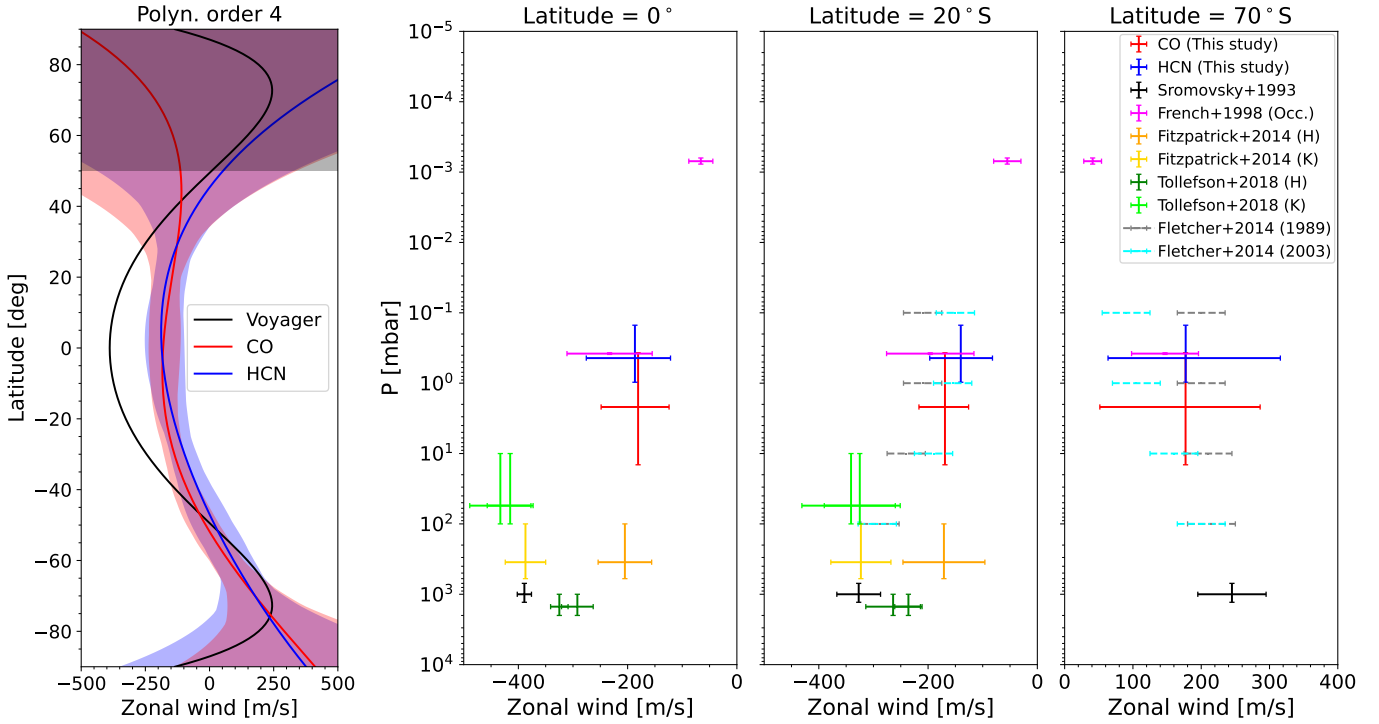
Fig. 3. Retrieval results. Left: retrieved best-fitting wind profiles for CO (red line) and HCN (blue line) measurements, using a fourth-order polynomial. Red and blue shadowed regions contain the ensemble of good fits according to the χ^2 criterion from Eq. (3). The semi-transparent grey rectangle indicates the unobservable northern latitudes. The solid black line shows the sixth-order fit to Voyager's cloud-tracking winds (Sromovsky et al. 1993). Right: wind variations with altitude at the equator, 20°S and 70°S, both for our measurements and for a set of references in the literature (see Sect. 5 for details). Cloud-tracking winds from Fitzpatrick et al. (2014) and Tollefson & Pater (2018) are not shown at 70°S as they have uncertainties of about $1000\,\mathrm{m\,s^{-1}}$. Winds from Fletcher et al. (2014) do not correspond to a direct measurement, but to the computed thermal wind equation applied to a reanalysis of the 1989 IRIS/Voyager data (dashed grey lines) and to 2003 Keck data (dashed cyan lines).

Our equatorial wind is about $200^{+100}_{-80}\,\mathrm{m\,s^{-1}}$ less intense than the Voyager reference. Assuming nominal probed levels of ~1 mbar and ~1 bar, respectively, this indicates a $+70^{+30}_{-20}\,\mathrm{m\,s^{-1}}$ wind shear per pressure decade (or $\partial u/\partial z = +30 \pm 10\,\mathrm{m\,s^{-1}}$ per scale height), where the positive sign is related to the retrograde wind direction. At 70°S, our winds are about $70^{+180}_{-170}\,\mathrm{m\,s^{-1}}$ less intense than Voyager's. We find a much smaller wind shear at 70°S, although the uncertainties are larger than for equatorial winds: $-20 \pm 60\,\mathrm{m\,s^{-1}}$ per pressure decade (or $\partial u/\partial z = -9 \pm 25\,\mathrm{m\,s^{-1}}$ per scale height). Our results compare well with the estimates from French et al. (1998, their Fig. 11b), who studied the wind-shear between Voyager's cloud-tracking winds (which they assumed at 100 mbar) and their occultation data at 0.38 mbar. French et al. (1998) determined a wind shear of about $+30\,\mathrm{m\,s^{-1}}$ per scale height at the equator and $-15\,\mathrm{m\,s^{-1}}$ per scale height at 70°S.

In contrast, cloud-tracking measurements from Tollefson & Pater (2018) appear somewhat at odds with our estimated wind shear, as their H-band measurements – assumed by the authors to probe deeper levels – indicate less intense winds than the K' band. Tollefson & Pater (2018) assumed that the H-band (resp. K') winds probe the 1–2 bar (resp. 10–100 mbar) level. This led them to an inverted wind shear, with the equatorial winds becoming more intense with increasing altitude. The authors attempted to explain this behavior by invoking a thermal-compositional wind equation that accounts for density changes associated to latitudinal variations of the methane abundance. We find that such an approach is not warranted according to our results. Furthermore, the absolute sounded pressures are uncertain and highly model-dependent

and both bands might not be probing such different pressure levels (Tollefson & Pater 2018, Fig. 16 therein). Similarly, Fitzpatrick et al. (2014) found differences among their cloud-tracking H- and K'-band winds. The pressure levels of the observed clouds are also uncertain in this case, with both H- and K'-band clouds spanning pressure levels between 0.1 and 0.6 bar (Fitzpatrick et al. 2014, Fig. 11 therein).

In itself, the consistency of our direct wind measurements with thermal wind calculations does not highlight a particular mechanism responsible for the wind decay with altitude; namely, the thermal wind equation simply states a balance between vertical wind shears and temperature meridional gradients. The wind decay reported here indicates a drag source, which could be the propagation and breaking of gravity and/or planetary waves (common in planetary stratospheres), although this has to be tested in dynamical simulations. On Saturn and Jupiter, interactions between vertically-propagating waves and the mean zonal flow drive the strong acceleration and deceleration of the stratospheric equatorial zonal flow (e.g., Cosentino et al. 2017; Bardet et al. 2022). Wave-breaking as a source of friction was also hypothesized by Ingersoll et al. (2021) to maintain the stacked circulation cells in Jupiter's upper troposphere.

Our measurements open up a new window on the study of Neptune's stratospheric dynamics. In addition, our findings provide useful information for general-circulation modelling studies (Liu & Schneider 2010; Milcareck et al. 2021), which require observations to compare with the numerical simulations. Nevertheless, our wind measurements remain modest in precision, as a result of combined limited integration time and low spatial resolution. Future dedicated observations, possibly combined with

long-term monitoring (given the duration of Neptune seasons), are expected to yield further insights into the topic.

References

Bardet, D., Spiga, A., & Guerlet, S. 2022, Nat. Astron., 6, 804
Benmahi, B., Cavalié, T., Fouchet, T., et al. 2022, A&A, 666, A117
Cavalié, T., Billebaud, F., Encrenaz, T., et al. 2008, A&A, 489, 795
Cavalié, T., Benmahi, B., Hue, V., et al. 2021, A&A, 647, L8
Conrath, B., Flasar, F. M., Hanel, R., et al. 1989, Science, 246, 1454
Cordiner, M. A., Garcia-Berrios, E., Cosentino, R. G., et al. 2020, ApJ, 904, L12
Cosentino, R. G., Morales-Juberías, R., Greathouse, T., et al. 2017, J. Geophys. Res. (Planets), 122, 2719
de Pater, I., Fletcher, L. N., Luszcz-Cook, S., et al. 2014, Icarus, 237, 211
Fitzpatrick, P. J., de Pater, I., Luszcz-Cook, S., Wong, M. H., & Hammel, H. B. 2014, Ap&SS, 350, 65
Fletcher, L. N., de Pater, I., Orton, G. S., et al. 2014, Icarus, 231, 146
Fletcher, L. N., Kaspi, Y., Guillot, T., & Showman, A. P. 2020, Space Sci. Rev., 216, 30
Foreman-Mackey, D., Hogg, D. W., Lang, D., & Goodman, J. 2013, PASP, 125, 306
French, R. G., McGhee, C. A., & Sicardy, B. 1998, Icarus, 136, 27
Goodman, J., & Weare, J. 2010, Commun. Appl. Math. Comput. Sci., 5, 65
Hammel, H. B., Beebe, R. F., de Jong, E. M., et al. 1989, Science, 245, 1367

Helled, R., Anderson, J. D., & Schubert, G. 2010, Icarus, 210, 446
Högbom, J. A. 1974, A&AS, 15, 417
Hueso, R., de Pater, I., Simon, A., et al. 2017, Icarus, 295, 89
Ingersoll, A. P., Atreya, S., Bolton, S. J., et al. 2021, Geophys. Res. Lett., 48, e2021GL095756
Irwin, P. G. J., Teanby, N. A., Davis, G. R., et al. 2011, Icarus, 216, 141
Irwin, P. G. J., Fletcher, L. N., Tice, D., et al. 2016, Icarus, 271, 418
Karkoschka, E. 2011, Icarus, 215, 439
Lecacheux, A., Zarka, P., Desch, M. D., & Evans, D. R. 1993, Geophys. Res. Lett., 20, 2711
Lellouch, E., Goldstein, J. J., Bougher, S. W., Paubert, G., & Rosenqvist, J. 1991, ApJ, 383, 401
Lellouch, E., Gurwell, M. A., Moreno, R., et al. 2019, Nat. Astron., 3, 614
Lellouch, E., Paubert, G., Moreno, R., & Moullet, A. 2008, Planet. Space Sci., 56, 1355
Limaye, S. S., & Sromovsky, L. A. 1991, J. Geophys. Res., 96, 18941P
Liu, J., & Schneider, T. 2010, J. Atmos. Sci., 67, 3652
Luszcz-Cook, S. H., de Kleer, K., de Pater, I., Adamkovics, M., & Hammel, H. B. 2016, Icarus, 276, 52
Milcareck, G., Guerlet, S., Spiga, A., et al. 2021, European Planetary Science Congress, EPSC2021-54.
Moreno, R., Marten, A., & Hidayat, T. 2005, A&A, 437, 319
Moreno, R., Lellouch, E., Forget, F., et al. 2009, Icarus, 201, 549
Moreno, R., Lellouch, E., Cavalié, T., & Moullet, A. 2017, A&A, 608, L5
Orton, G. S., Encrenaz, T., Leyrat, C., Puetter, R., & Friedson, A. J. 2007, A&A, 473, L5
Press, W. H., Teukolsky, S. A., Vetterling, W. T., & Flannery, B. P. 2007, Numerical Recipes: The Art of Scientific Computing, 3rd edn. (USA: Cambridge University Press)
Smith, B. A., Soderblom, L. A., Banfield, D., et al. 1989, Science, 246, 1422
Sromovsky, L. A., Limaye, S. S., & Fry, P. M. 1993, Icarus, 105, 110
Sromovsky, L. A., Fry, P. M., Dowling, T. E., Baines, K. H., & Limaye, S. S. 2001a, Icarus, 149, 459
Sromovsky, L. A., Fry, P. M., Dowling, T. E., Baines, K. H., & Limaye, S. S. 2001b, Icarus, 150, 244
Tollefson, J., de Pater, I., Marcus, P. S., et al. 2018, Icarus, 311, 317
Warwick, J. W., Evans, D. R., Peltzer, G. R., et al. 1989, Science, 246, 1498
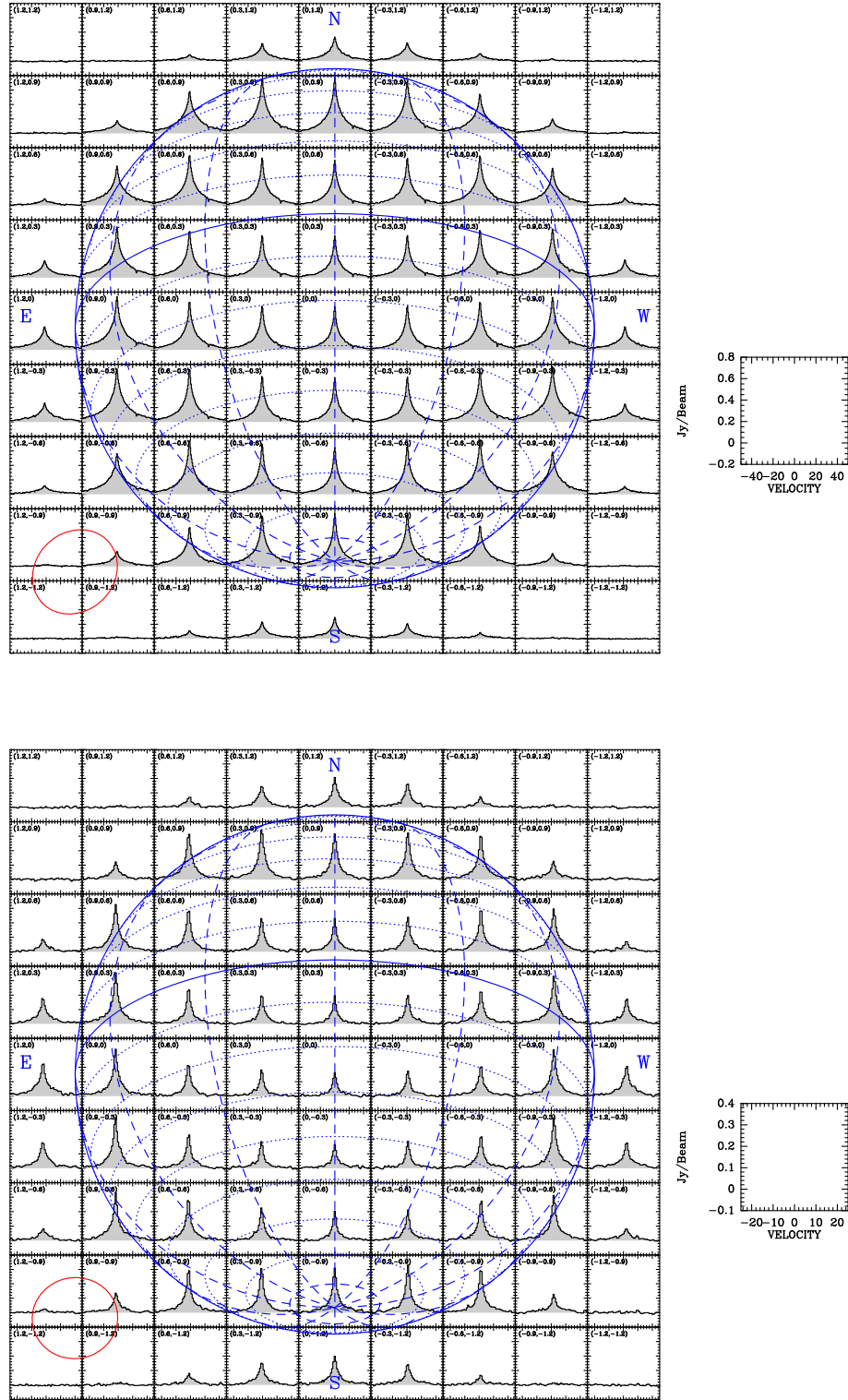
Appendix A: Measured spectral maps

Fig. A.1. Measured spectral maps. Top: Spectral map of the CO(3–2) transition at 345.796 GHz on Neptune observed on April 30, 2016 with ALMA (top row). The spectral resolution is 1 MHz. The planet's angular diameter is 2.24″ and is shown by a blue circle. The synthesized beam is indicated with a red ellipse. The right box represent the scales of the spectra expressed in flux (Jy/beam) against velocity (km s^{-1}). Bottom: Spectral map of the HCN(4–3) transition at 354.505 GHz, measured simultaneously with that of CO.

Appendix B: Parameterizing wind profiles with different polynomial orders
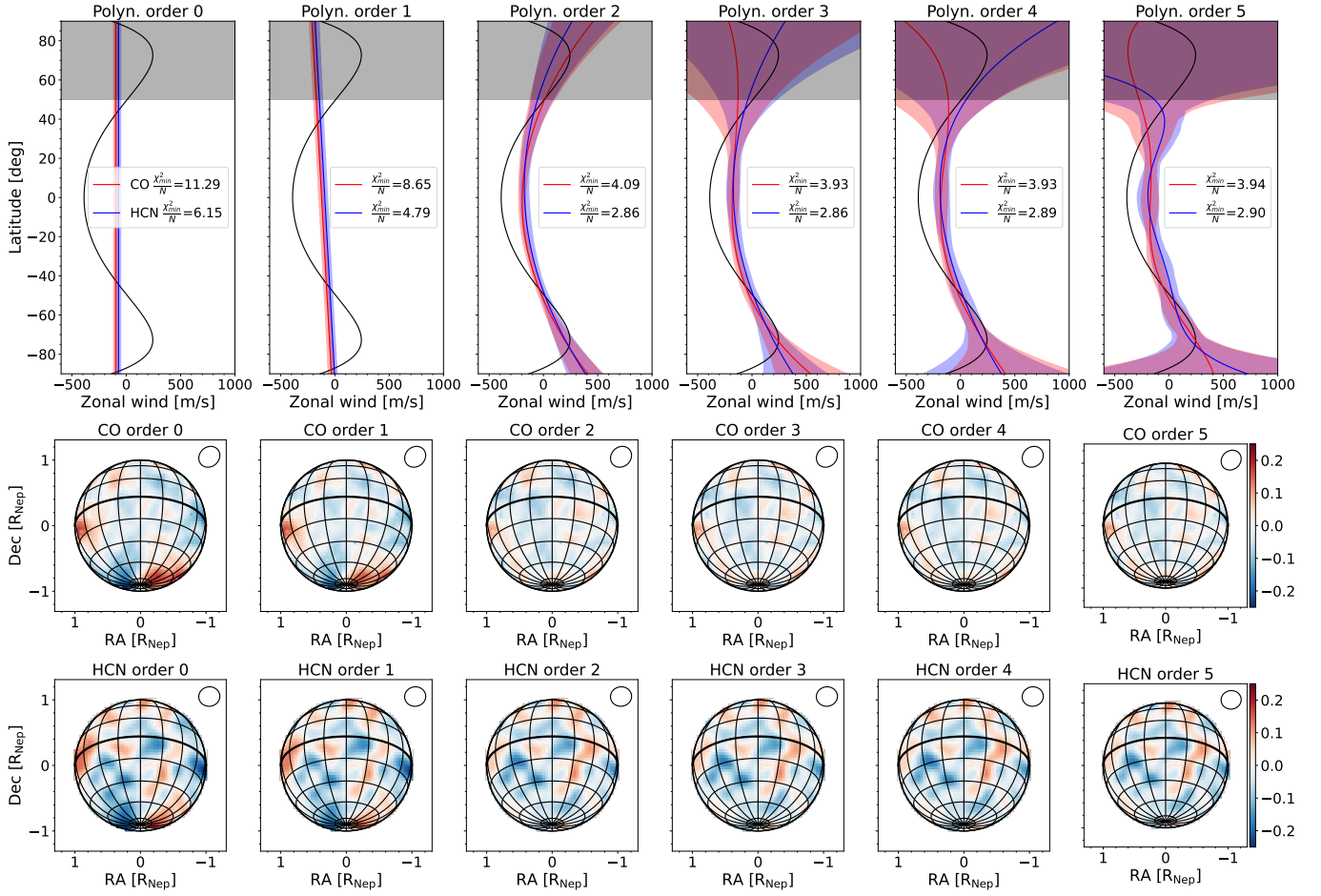

Fig. B.1. As in Fig. 3, top row shows the retrieved wind profiles for CO and HCN, but using different polynomial orders for the wind parameterization. The value of χ^2_{min}/N is shown in the legend. We also show the residual maps of CO (middle row) and HCN (bottom row) after subtracting the best-fitting wind profile to the measurements.